Microwave Plasmonic Exceptional Points for Enhanced Sensing

Zhen Liao, Xing Peng, Leilei Liu,, Yihao Xu, Kai-Da Xu, Baicao Pan, Guo Qing Luo,,* and Yongmin Liu**

The emergence of exceptional points in a non-Hermitian system has provided intriguing possibilities to enhance the sensitivity of a sensor, while it is yet a considerable challenge to implement subwavelength non-Hermitian systems. One possible solution to tackle this challenge is to take advantage of localized surface plasmon resonances, which enable large electromagnetic enhancement at the subwavelength scale. In this work, a novel sensing scheme based on the exceptional points in a spoof plasmonic structure working at microwave frequencies is proposed. It is shown that near-field plasmonic vortices can be efficiently generated at the exceptional points, resulting in the enhanced sensitivity when detecting a single particle or fluid analytes. Single particle detection with the particle size as small as 1/100 of the operating wavelength is reported. For liquid analysis in the microfluidic system, the sample consumption is down to 0.72 μL. This work demonstrates the ultrahigh sensitivity of exceptional-point-based plasmonic sensing and opens up new possibilities for subwavelength and compact sensors operating in the microwave, terahertz, and even far-infrared regions.

1. Introduction

Recently, non-Hermitian physics has been investigated in various settings like acoustics,[1] mechanics,[2] electromagnetism,[3] and atomic systems.[4–6] Such open systems with loss and/or gain exhibit a singularity known as an exceptional point (EP), at which two or more eigenstates become degenerated and so do their eigenvalues.[7] Tremendous efforts have been devoted to the study of non-Hermitian systems and their exotic effects. Around the EP, the system topology can be manipulated to produce unusual phenomena, such as unidirectional invisibility,[8–10] asymmetric mode switching,[11] and directional lasing.[12] Moreover, enhanced sensitivity is one very promising application of non-Hermitian physics. For trace analytes, the sensitivity of EP-based sensors can be boosted by orders of magnitude.[13] For example, EP-enhanced sensitivity was confirmed for detecting a single nanoparticle using the whispering gallery mode in a micro-toroid cavity.[14] A non-Hermitian photonic sensor based on a microring resonator exhibits an exceptional hypersurface, enabling robustness together with an enhanced sensitivity.[15] While the rich physics and applications of non-Hermitian systems have been explored, their implementations are usually based on large-scale structures. Recently, metasurfaces with subwavelength elements have facilitated the study of non-Hermitian systems and enriched the related applications.[16–18] Plasmonic metasufaces,

Z. Liao, L. Liu,
National and Local Joint Engineering Laboratory of RF Integration and Micro-Assembly Technology, College of Electronic and Optical Engineering & College of Flexible Electronics (Future Technology)
Nanjing University of Posts and Telecommunications
Nanjing 210003, China
E-mail: liull@njupt.edu.cn

Z. Liao, X. Peng, B. Pan, G. Q. Luo,
Key Laboratory of RF Circuits & System of Ministry of Education, School of Electronics and Information
Hangzhou Dianzi University, Xiasha High Education Park
Hangzhou 310018, China
E-mail: luoguoqing@hdu.edu.cn

Y. Xu
Department of Mechanical and Industrial Engineering
Northeastern University, Boston
MA 02115, USA

K.-D. Xu
School of Information and Communications Engineering
Xi'an Jiaotong University
Xi'an 710049, China

Y. Liu
Department of Mechanical and Industrial Engineering
Department of Electrical and Computer Engineering, Northeastern University, Boston
MA 02115, USA
E-mail: y.liu@northeastern.edu

in particular, present a viable solution for achieving subwavelength non-Hermitian systems, effectively shrinking the device footprint for practical applications.[19] The symmetry-breaking-induced plasmonic EP based on the hybridization of detuned resonators has been demonstrated in a multilayered periodic plasmonic structure, which enables enhanced sensing of anti-immunoglobulin G (IgG).[20]

Detecting small objects, single molecules, or individual nanoparticles has numerous prospects in various fields, such as biomedical analysis and disease diagnosis. Over the past decades, many techniques have been developed, including single-molecule fluorescence methods,[21] photothermal microscopy,[22] and optical microresonators.[23] Among them, the label-free plasmonic sensors based on metallic nanostructures have attracted considerable research interest since the collective oscillation of electrons in metals, called localized surface plasmon resonance (LSPR), can produce large electromagnetic near-field enhancement.[24,25] The local fields evanescently decay from the metal surface. Therefore, the sensor only probes a nanoscale region around the metallic structures. This highly localized sensing volume allows one to observe molecular interactions near the nanoparticle surface.[26,27] In addition, the use of nanoparticles implies a vastly reduced sensor volume, which is an attractive aspect for miniaturized sensors. The EP-based LSPR sensor is expected to combine the advantages of plasmonics and non-Hermitian physics to realize an ultrasensitive and compact subwavelength sensor for small object or trace analyte detection.

LSPR is typically limited to the visible and near-infrared regions. Recently, researchers have developed periodically textured metallic meta-structures to support spoof LSPR at low frequencies (i.e., microwave, terahertz, or far-infrared).[28] It mimics optical LSPR with tailored resonance frequencies, which depend on the geometric parameters of the subwavelength corrugation. Many interesting studies of spoof plasmonics with distinct meta-structures have been reported. For example, at microwave frequencies, plasmonic vortex modes can be generated by a subwavelength spoof-LSPR-based meta-particle.[29–31] Free-space microwave vortex modes can be produced by exciting spoof surface plasmons in a resonator antenna.[32,33] Besides, electromagnetic skyrmions can be constructed by the electric and magnetic field vectors of spoof LSPR.[34–36] At THz frequencies, orbital angular momentum (OAM) beams have been selectively transferred from vortex beams to spoof LSPR in a sub-diffraction-limited meta-particle.[37]

In this work, we demonstrated an EP in a spoof LSPR system by exploiting a deep subwavelength meta-particle with non-Hermitian scattering. Here, we introduced two perturbations in the meta-particle. We found that the coupling between two plasmonic vortices could be tuned by varying the relative positions and the strength of the perturbations.[13] Afterward, this coupling was used to implement the EP. A proof-of-concept demonstration at microwave frequencies was conducted. In our simulations and experiments, we achieved coalesced microwave plasmonic vortices at the EP in a single subwavelength LSPR meta-particle. Compared with conventional LSPR sensors, the proposed LSPR meta-particle sensor utilizing non-Hermitian physics promises ultrahigh sensitivity for a sufficiently small object, pushing the detection limit down to 1/100 of the operating wavelength. Moreover, employing EP-based LSPR sensors facilitated the detection

of liquids within a microfluidic channel. The advantages of these sensors became apparent, particularly when working with small volumes of liquid samples (0.72 µL). The proposed scheme paves the way for subwavelength compact sensors that can be widely used in physical chemistry, materials science, and bioscience.

2. The EP System

Let us start with the textured copper disk shown in **Figure 1**a, which supports spoof LSPR. In the context of metamaterials, when the width of grooves is much smaller than the operating wavelength, the region with grooves can be modeled as an effective medium.[28] The effective properties depend on the geometrical parameters of the structure. A uniformly corrugated cooper disk behaves as a copper cylinder coated with a layer of anisotropic metamaterial, as illustrated in Figure 1b. The resulting spoof LSPR and field enhancement are in analogy to conventional LSPR in the optical region.[28] Due to its circular geometry, the corrugated disk supports two spoof LSPR modes that propagate in the clockwise (CW) and counterclockwise (CCW) directions and carry OAM with opposite topological charges.[29,31] Moreover, the meta-particle supports orthogonal eigenstates at the degenerated eigenfrequency, which is known as the diabolic point (DP, see Section S1 in the Supporting Information for details). In such a system, if the spoof LSPR mode is perturbed, its eigenvalue splitting is linearly proportional to the perturbation strength.[14]

On the other hand, a nonuniformly textured metallic disk can be considered as a copper cylinder coated with an anisotropic metamaterial layer while a perturbation exists. The perturbation induces coupling between the CW and CCW traveling modes due to the backscattering. The coupled-mode equations of the system can be written as

$$-i\frac{d}{dt}\begin{pmatrix} a_l \\ a_{-l} \end{pmatrix} = \begin{pmatrix} \Omega & A \\ B & \Omega \end{pmatrix} \begin{pmatrix} a_l \\ a_{-l} \end{pmatrix} = H\begin{pmatrix} a_l \\ a_{-l} \end{pmatrix} \tag{1}$$

In Equation (1), a_l (a_{-l}) is the complex amplitude of the plasmonic vortex carrying OAM with the topological charge of l ($-l$). H is the Hamiltonian that describes the energy of the whole system. The real part of Ω is the frequency and the imaginary part is the decay rate of the plasmonic vortex, respectively. A (B) is the backscattering strength from the vortex mode of $-l$ (l) to l ($-l$). The system approaches EP when coefficient A or B vanishes, indicating that the coupling between the two plasmonic vortex modes becomes unidirectional. In this case, the Hamiltonian has not only degenerated eigenvalues but also a single coalesced eigenstate copropagating in the same direction.

Here, two teeth of the spoof LSPR meta-particle are extended as perturbations to tune the backscattering of plasmonic vortices and hence steer the system to an EP (Figure 1c,d). The characteristic of the structure is numerically and experimentally evaluated by exciting the LSPR with a spoof surface plasmon polaritons (SSPP) waveguide (see Section S2 in the Supporting Information for details). The waveguide and corrugated disk are printed on a 1 mm thick F4b circuit board with a relative permittivity of 2.55, as shown in **Figure 2**a. The inner radius r is set as 3 mm. The width a and periodicity d of the groove at the periphery of the disk are 0.47 and 0.94 mm, respectively. The number of grooves
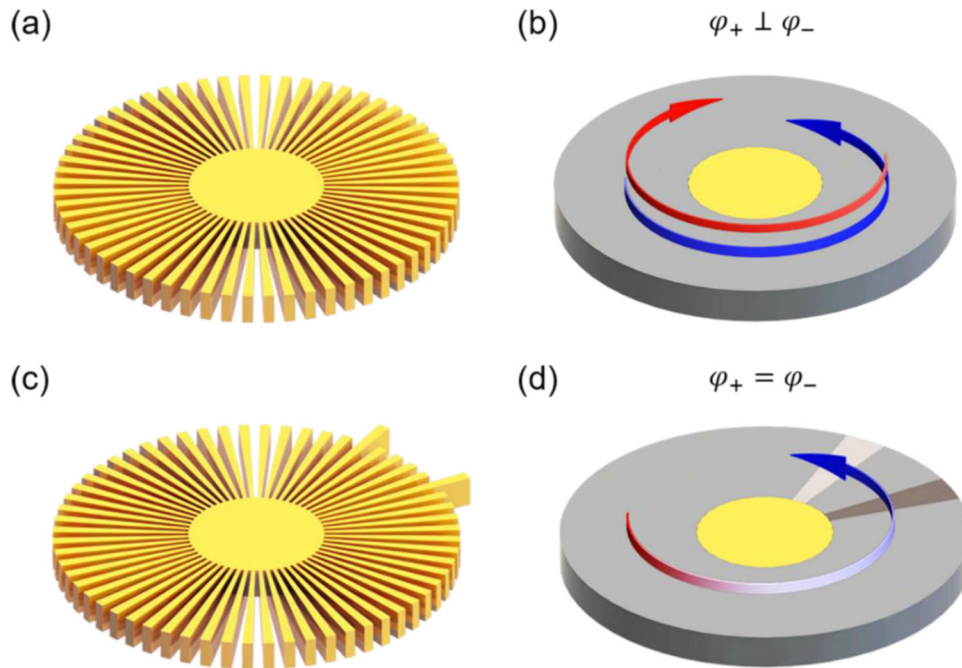
Figure 1. a) Schematic of a uniformly corrugated copper disk. b) Under the effective medium approximation, the structure in (a) behaves as a cooper cylinder coated with a layer of anisotropic metamaterial, which supports two counterpropagating eigenstates ($\varphi+$ and φ). c) Schematic of a corrugated copper disk with two extended teeth. d) The two eigenstates coalesce for the disk with two perturbations when operating at an EP.
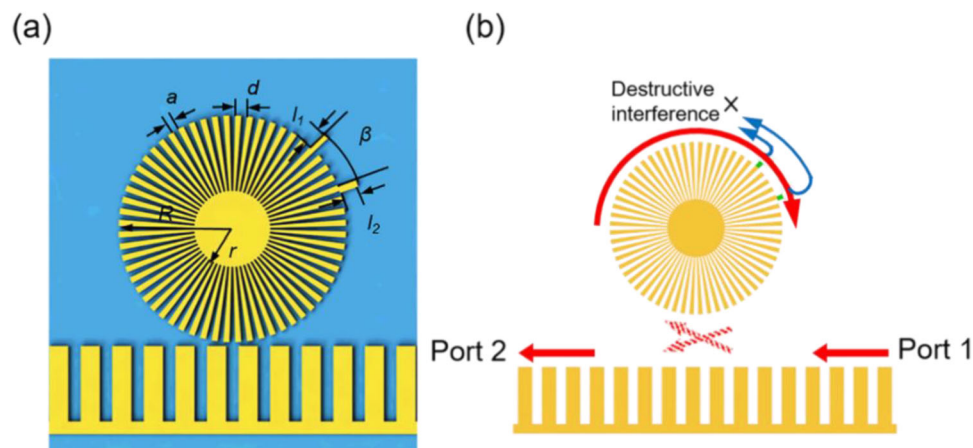

Figure 2. a) Schematic diagram of the proposed plasmonic structure. b) Equivalent model revealing the mechanism of coalesced eigenvalues, which can be understood from the completely destructive interference between the backscattered CCW waves from the two protruded teeth.

is chosen as 60. Note that the outer diameter of the meta-particle R is 18 mm, which is only 3/8 of the operating wavelength. The equivalent model of the system is shown in Figure 2b. The surface waves are coupled from the SSPP waveguide to the spoof LSPR resonator through the phase- and mode-matched power exchange. When the CW traveling surface waves on the metaparticle encounter the extended teeth, backscattered waves arise (denoted by the blue arrows in Figure 2b). If the two backscattering waves acquire destructive interference and cancel out each other, a unidirectional plasmonic vortex mode can be produced.

In our design, we first fixed the extended radial comb $l_1 = 1.5$ mm. We adjusted the second extruded comb to tune the sys-

tem to approach the EP, which can be identified by the coalescence of the frequency eigenvalues and the corresponding eigenstates. We have conducted numerical simulations to investigate the effect of the length l_2 and the relative angular position β of the second extended tooth on the transmission spectra by varying the two parameters. The results are depicted in **Figure 3**. Figure 3a presents the transmission spectrum with the extended length l_2 changed from 1 to 1.9 mm, when the relative angular position β is 0.44 rad. As l_2 increases, the frequency splitting becomes less significant. Subsequently, the crossing of resonance frequencies occurs, meaning that the eigenvalues overlap near the specific length $l_2 = 1.5$ mm. In Figure 3b, when l_2 is fixed as 1.5 mm,
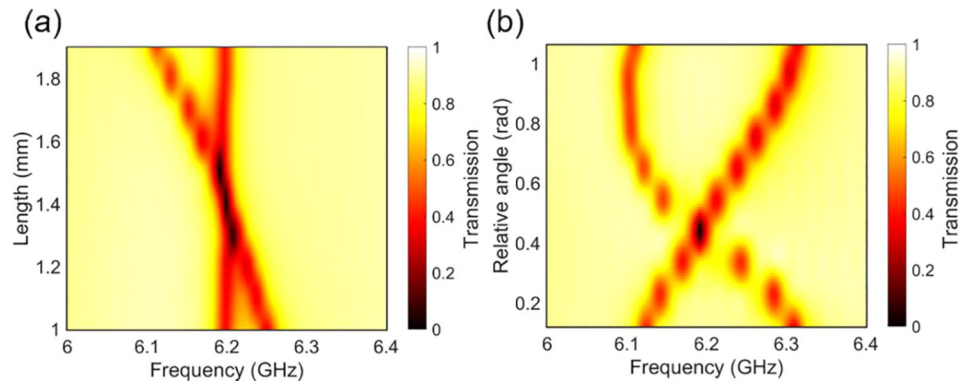
Figure 3. Transmission spectra when varying a) the length, and b) the relative angle of the second extended tooth.
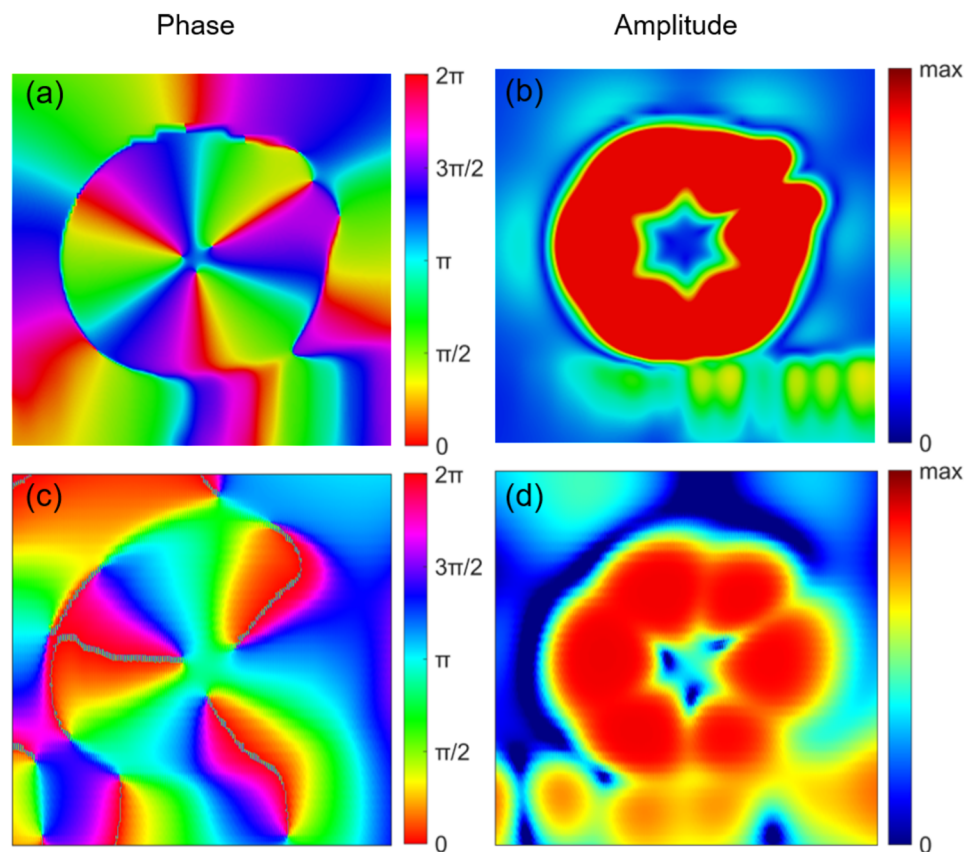
Figure 4. a) Simulated phase and b) amplitude distributions of the E_z component for the CW plasmonic vortex at the EP. The plots are in the plane 2 mm above the meta-particle. c) Measured phase and d) amplitude distributions at the EP.

the position of the second comb determines the frequency splitting. Starting with 0.12 rad, the frequency difference between the two modes reduces as β increases. Then a single resonance is observed in the transmission spectrum with $\beta = 0.44$ rad. When β further increases, the frequencies split again. Therefore, we can conclude that the eigenvalue degeneration occurs at 6.19 GHz with $\beta = 0.44$ rad and $l_2 = 1.5$ mm, implying the EP of the system.

The presence of EP not only leads to a perfect spectral overlap between the resonances, but also forces the two corresponding plasmonic vortex modes to be identical. To present the interesting behavior at the EP, we plot the simulated phase of the E_z component at the degenerated frequency 6.19 GHz in **Figure 4**a, clearly showing a continuous phase change along the azimuthal direction by 6π upon one full circle around the center. Figure 4b shows the simulated amplitude of the E_z component. The amplitude profile remains almost unchanged along the outer circle, where no interference pattern emerges within the meta-particle. These results demonstrate that a plasmonic vortex wave carrying angular momentum of $l = 3$ travels along the azimuthal direction.

They also imply that the plasmonic vortex waves are copropagating as eigenmodes at the EP, due to the destructive interference between the backscattering induced by the two perturbations as illustrated in Figure 2b. The experimentally measured results are shown in Figure 4c,d, which agree very well with the simulations. The measurement setup to map the near fields is described in Section S3 in the Supporting Information. In addition, the plasmonic vortex modes of $l = 2$ and 4 at other EPs are presented in Section S4 in the Supporting Information.

For comparison, we also measured the transmission of a textured disk with a single extended comb, as shown in Section S5 in the Supporting Information (Figure S5a, Supporting Information). Frequency splitting is clearly seen in the transmission spectrum. The two dips in the spectrum correspond to the two eigenvalues and eigenstates of the system arising from the coupling between the opposite vortices (Figure S5b, Supporting Information). The electric field distributions at the two resonance frequencies (Figure S6, Supporting Information) exhibit very different behaviors, in comparison to the plasmonic vertex at the EP. The near-field results clearly show standing wave patterns, resulting from the coexistence of the CW and CCW modes in the meta-particle.[29]

3. Enhanced Sensing

An important application of LSPR is the detection of a single nanoparticle or biomolecule. In a conventional sensing system operating around a DP, the resulting eigenvalue splitting is linearly proportional to the perturbation strength ϵ. On the contrary, the complex frequency splitting of an EP sensor $\Delta\omega_{EP}$ subject to the same perturbation can be expressed as

$$\Delta\omega_{EP} = 2\epsilon\sqrt{1 + \frac{A^{(2)}e^{i2m\beta}}{\epsilon}} \cong 2\sqrt{A^{(2)}e^{i2m\beta}\epsilon} \tag{2}$$

where $A^{(2)}$ indicates the intrinsic backscattering in the sensor at the EP,[13,14] m denotes the azimuthal mode number, and β is the angular position of the target scatterer. The frequency splitting is proportional to the square-root of a small perturbation strength ϵ, when $A^{(2)}$ is much larger than ϵ (see Section S1 in the Supporting Information). Therefore, the EP-based LSPR is expected to provide enhanced sensitivity for a single small object.
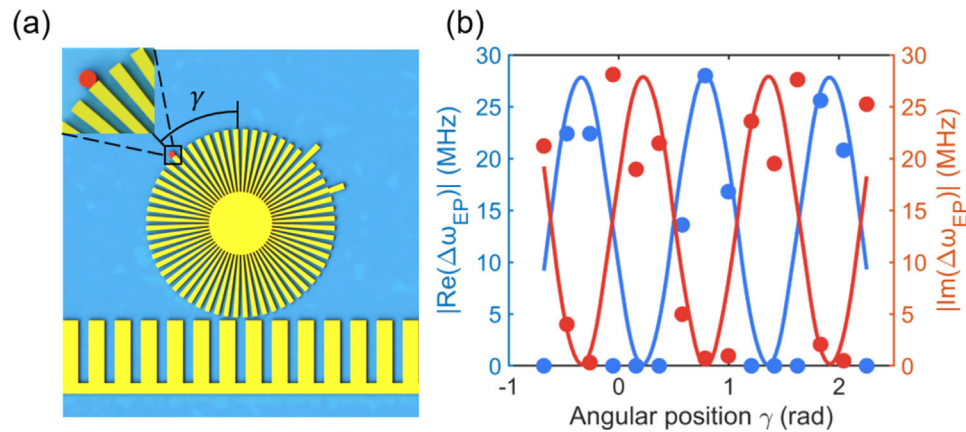
Here, we demonstrate a compact EP-based LSPR sensor to detect a deep-subwavelength object. We have evaluated the Q-factor of EP modes carrying OAM with topological charges of 2, 3, and 4 based on the transmission spectra (Figure 6b and Section S4 in the Supporting Information). The obtained Q-factor values are 211, 282, and 237, respectively. Notably, the EP mode with a topological charge $l = 3$ exhibits the highest Q-factor. Additionally, the Q-factor and resonance intensity are the key parameters for sensing, as they determine the sensitivity of the structure. We introduce the figure of merit (FoM) as a metric considering both the Q-factor and resonance intensity, which is given by FoM $= Q \times \delta I$.[38] Here Q represents the quality factor and δI corresponds to the resonance amplitude of the EP resonance mode. For the topological charges of 2, 3, and 4, the FoM values are 139, 250, and 210, respectively. Remarkably, the FoM reaches its maximum value of 250 when $l = 3$. This indicates that the

EP mode with $l = 3$ provides the best compromise between high resonance intensity and superior energy dissipation characteristics. Based on these findings, we can conclude that the EP mode with $l = 3$ is the most suitable candidate for our sensing applications. Its exceptional FoM and high Q-factor ensure enhanced sensitivity and reliable sensing capabilities.

We use a metallic circular patch (0.6 mm in diameter) as the object to be detected, which perturbs the copropagating plasmonic vortices (**Figure 5**a). Subsequently, the system deviates from the EP, giving rise to complex frequency splitting. We have studied the dependence of the complex frequency splitting on the relative angular position γ of the object, as shown in Figure 5b. The complex frequency information is extracted by fitting the transmission spectra using a doublet Lorentz model (see Section S6 in the Supporting Information).[39] The blue and red dots represent the real and imaginary parts of the complex frequencies when the angular position of the object is changed. It is found that the frequency splitting (real part) and the difference in linewidth (imaginary part) alternate periodically between maximum and minimum. The maximum frequency splitting corresponds to the minimum linewidth difference, while the absolute value remains constant. The theoretically fitted curve could be obtained by using sine function, corresponding to the solid curves in Figure 5b. These results agree well with the predictions from Equation (2). To observe complex frequency splitting conveniently, we put the detected object at a special position with $\gamma = 0.79$ rad, where the linewidth difference equals zero. It means that the frequency splitting Re($\Delta\omega_{EP}$) can represent the magnitude of the complex frequency splitting, i.e., $|\Delta\omega_{EP}|$.

For a better comparison, we have simulated the transmission spectra of the DP and EP sensor before adding the small object in **Figure 6**a,b, respectively. Both of them show a single resonance frequency. Then we compare the sensitivity of the EP sensor with the DP sensor in the presence of the circular patch (0.6 mm in diameter) as the analyte. Figure 6c,d plots the spectra of the conventional DP sensor and the proposed EP sensor, respectively. The EP sensor shows an obvious frequency splitting of 28 MHz, while the frequency splitting of the DP sensor is only about 12.8 MHz. This result strongly indicates that the EP sensor exhibits higher sensitivity than the DP sensor for a small object.

We further evaluate the sensitivity for objects with different sizes through the spectral responses of the EP and DP sensors (see Section S7 in the Supporting Information). **Figure 7**a displays the simulated resonance splitting for the EP and DP sensors as histograms (red and blue, respectively). Starting with 1 mm, larger splitting for the DP sensor is first observed. We then progressively decrease the diameter of the detected object and observed the same splitting of resonance frequencies with a patch diameter of 0.92 mm. Then larger splitting of resonances occurs in the EP sensor compared to the DP sensor for a patch diameter smaller than 0.92 mm. The result confirms that the proposed EP sensor indeed becomes more sensitive when the analyte is small. We further reduce the patch diameter, and notice that when the patch diameter is decreased from 0.56 to 0.48 mm, very interestingly, the frequency splitting of the DP sensor does not appear anymore. Although the frequency splitting of the DP system becomes undetectable in the transmission spectrum due to significant overlap of the resonance dips, the physical existence of frequency splitting remains. In sharp contrast, the splitting of

ADVANCED
SCIENCE NEWS

www.advancedsciencenews.com

LASER
& PHOTONICS
REVIEWS

www.lpr-journal.org

Figure 5. a) Illustration of an EP-based plasmonic sensor to detect a small metallic circular patch. b) Dependence of the complex frequency splitting on the angular position of the small object to be detected.
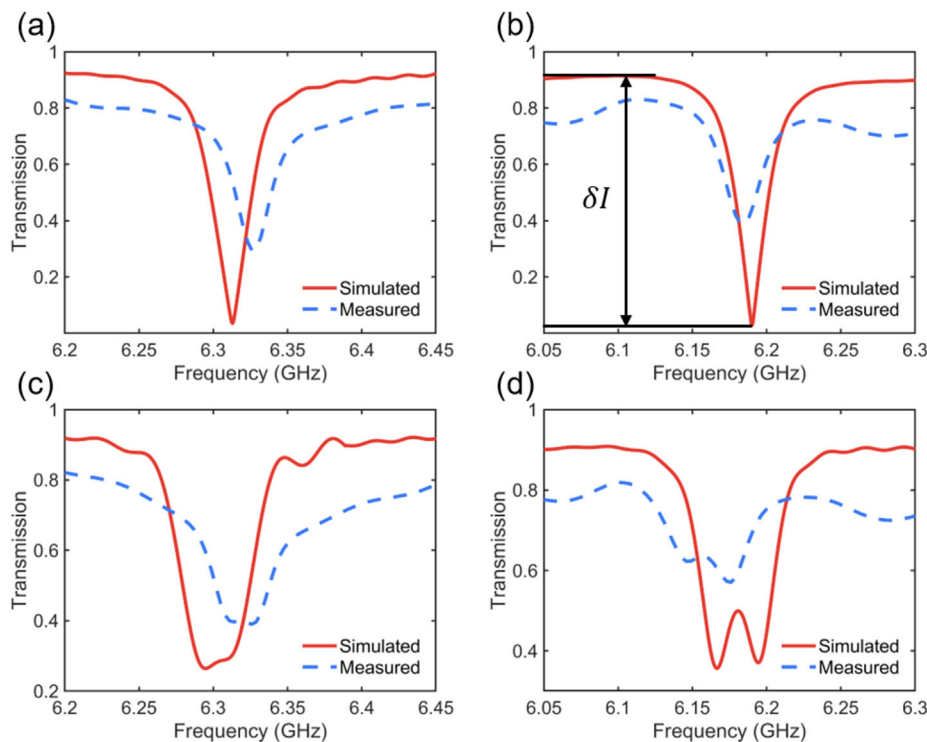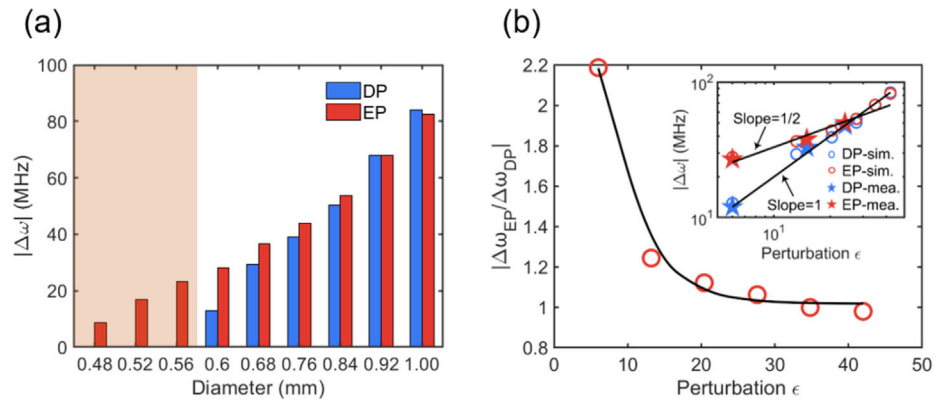

Figure 6. Simulated and measured transmission spectra of the a) DP and b) EP sensor without the object to be detected. δI in the figure corresponds to the resonance amplitude of the EP resonance mode. The transmission spectra of the c) DP and d) EP sensor after the object, a small patch, is introduced to the meta-particle.

the EP sensor is still obvious in this regime. It is worth noting that both sensors cannot identify the analyte with a patch diameter smaller than 0.48 mm (see Section S7 in the Supporting Information). These comprehensive studies lead to the conclusion that the smallest detectable object with our EP-based plasmonic system is 0.48 mm in diameter, about 1/100 of the working wavelength.

To further illustrate that the EP sensor has better performances for a sufficiently small object, the inset of Figure 7b shows the logarithmic plot of the relationship between resonance frequency splitting and analyte size that can be regarded as perturbation. The numerically simulated splitting for the DP sensor nicely follows a black line with a slope equal to 1. In contrast, the EP sensor exhibits a slope of 1/2 when the perturbation is smaller than 28 (corresponding to a patch diameter of about 0.84 mm). This trend is consistent with the theory prediction from Equation (2), which is proportional to $\sqrt{\varepsilon}$. Furthermore, the experimental results of the frequency splitting in the DP and EP sensors also follow a linear and square-root law, respectively, serving as a direct demonstration of DP-based and EP-based plasmonic sensors

ADVANCED
SCIENCE NEWS
www.advancedsciencenews.com

LASER
& PHOTONICS
REVIEWS

www.lpr-journal.org

Figure 7. a) Histograms presenting the simulated resonance splitting for the DP and EP sensors when the diameter of the circular patch is varied. b) Dependence of the complex frequency splitting $|\Delta\omega_{EP}/\Delta\omega_{DP}|$. The inset displays a logarithmic plot of the relationship between the resonance frequency splitting and the perturbation for the EP and DP sensors, respectively.
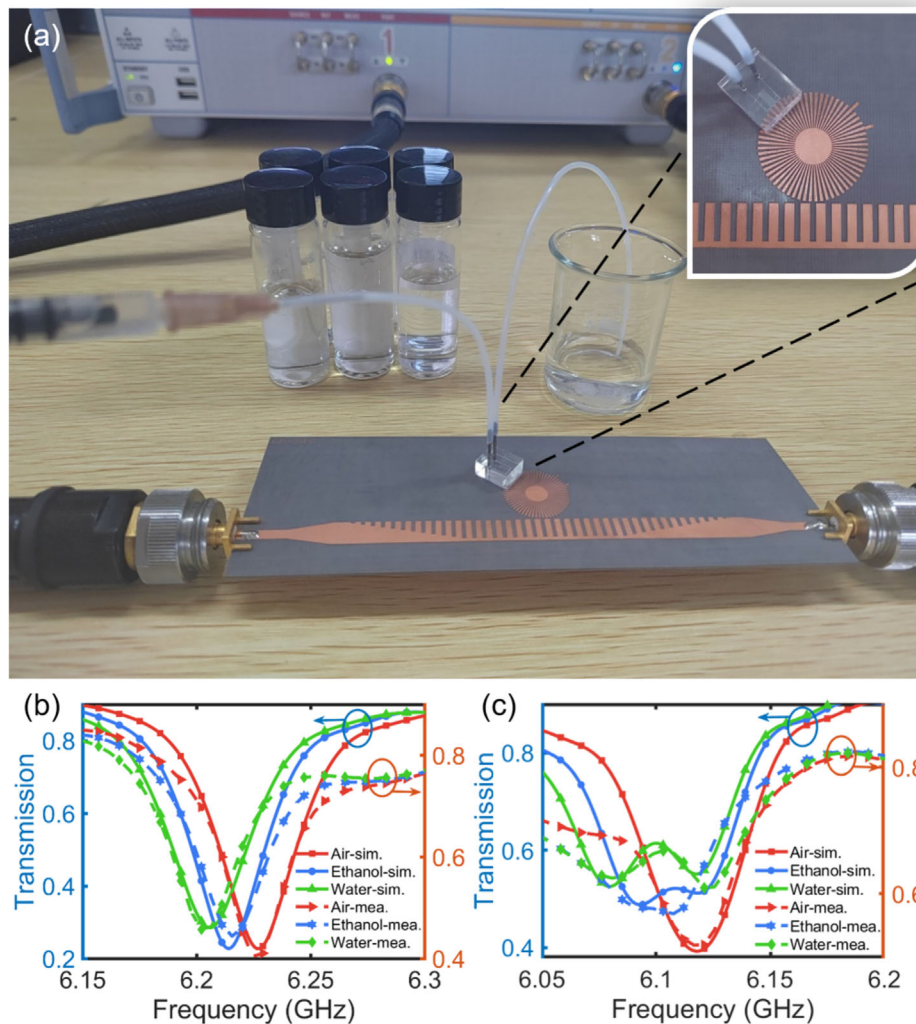
Figure 8. a) Measurement setup for liquid sensing based on an LSPR meta-particle that is integrated with a microfluidic chip. b) Transmission spectra with different fluid analytes for the DP sensor. c) Transmission spectra with different fluid analytes for the EP sensor.

(see inset of Figure 7b and Section S7 in the Supporting Information). In Figure 7b, we plot the complex frequency splitting ratio of the EP sensor to the DP sensor. We can see that the sensitivity of the EP sensor is 2.2 times higher than that of the DP sensor for sufficiently small perturbation. As the perturbation increases, the ratio approaches 1. Additionally, the effect of angular momentum number on the performance of the EP-based sensor is evaluated (see Section S8 in the Supporting Information).

The EP-based LSPR sensor also allows the analysis of fluid analytes down to a very small volume. The resonant frequency can be split by introducing a perturbation in the evanescent field of the edge. For this purpose, we have integrated the LSPR meta-particle with a microfluidic channel (see Section S9 in the Supporting Information for details). It is worth noting that the sample volume is down to 0.72 μL in the microfluidic channel. **Figure 8**a is the photograph of the measurement setup for liquid sensing. The thin plastic tubes and connector are inserted into the inlet and outlet of the polydimethyl siloxane (PDMS) microfluidic chip. Different analytes are injected into the tube through a syringe, and then flow through the microfluidic channel. The inlet is used to inject the analytes under test into the channel through a syringe, and the outlet is connected to a beaker for collecting the waste liquid. The inset of Figure 8a clearly shows the microfluidic channel integrated with the EP-based LSPR sensor. The transmission coefficient of the structure with the microfluidic channel is measured by using a vector network analyzer.

The sensing capabilities of EP and conventional DP LSPR sensors are then characterized with three kinds of analytes: air, ethanol, and water. Figure 8b,c shows the comparison of transmission coefficients of the DP sensor and EP sensor, respectively. When the channel is empty (i.e., air case), both sensors have only one resonance. Then we observe that no frequency splitting occurs for the DP sensor when the channel is filled with ethanol or water, whose refractive index is 26 and 78, respectively. However, regardless of the injected liquid, the transmission spectra of the EP sensor exhibit two pronounced resonance dips, indicating that the sensitivity is enhanced. The sensitivities of the EP-based LSPR sensor can be extracted from the frequency splitting, which are 25 and 38 MHz for the ethanol-filled and water-filled channels, respectively. Compared with the DP sensor, our EP-based LSPR sensing system has a better sensitivity of detecting 0.72 μL fluid analytes. The measurement results are consistent with the simulation results. Although our studies primarily focus on the microwave band, the strategy can be extended to terahertz and far-infrared frequencies by scaling the size of meta-structures.

4. Conclusion

We have demonstrated the EP in a microwave LSPR meta-particle via geometry-induced non-Hermitian mode coupling. The proposed subwavelength meta-particle creates degenerated eigenvalues and a coalesced plasmonic vortex at the EP. The meta-particle can take advantage of plasmonic enhancement and the ultrasensitive capacity of EP to measure small analytes with the size of only 1/100 of the wavelength, which is far beyond the conventional techniques. In addition, integrated with a microfluidic system, the EP-based LSPR sensor allows for sensing with an ultrasmall sample consumption down to 0.72 μL. We anticipate that our results will open a host of new possibilities for ultrasensi-

tive and subwavelength compact sensors for different disciplines, such as physical chemistry, materials science, and bioscience.

5. Experimental Section

Simulation and Numerical Methods: All of simulations were conducted with CST Studio Suite. Time-Domain Solver was used and open boundary conditions were applied in all directions of the sensor. And a field monitor was used to monitor the electric field at specific frequency points.

Experimental Methods: The transmission coefficients were measured by a vector network analyzer. The two ports of the vector network analyzer were connected to the two ends of the sensor. The electromagnetic wave was input from one port and output from the other port, and the instrument processes displayed the received signal. The near-field experiments were conducted in a microwave chamber. An electromagnetic wave was input into port one of the sensor, and a 50 Ω load was connected to port two. Then, the probe was used as the receiver to collect the electric field data by scanning each position in the plane 2 mm above the sample surface of the structure.

Supporting Information

Supporting Information is available from the Wiley Online Library or from the author.

Conflict of Interest

The authors declare no conflict of interest.

Data Availability Statement

The data that support the findings of this study are available from the corresponding author upon reasonable request.

[1] R. Fleury, D. Sounas, A. Alù, *Nat. Commun.* **2015**, *6*, 5905.
[2] C. M. Bender, B. K. Berntson, D. Parker, E. Samuel, *Am. J. Phys.* **2013**, *81*, 173.

[3] S. Bittner, B. Dietz, U. Günther, H. L. Harney, M. Miski-Oglu, A. Richter, F. Schäfer, *Phys. Rev. Lett.* **2012**, *108*, 024101.

[4] P. Peng, W. Cao, C. Shen, W. Qu, J. Wen, L. Jiang, Y. Xiao, *Nat. Phys.* **2016**, *12*, 1139.

[5] Z. Zhang, Y. Zhang, J. Sheng, L. Yang, M. A. Miri, D. N. Christodoulides, B. He, Y. Zhang, M. Xiao, *Phys. Rev. Lett.* **2016**, *117*, 123601.

[6] C. Hang, G. Huang, V. V. Konotop, *Phys. Rev. Lett.* **2013**, *110*, 083604.

[7] M. V. Berry, *Czech. J. Phys.* **2004**, *54*, 1039.

[8] L. Feng, Y. L. Xu, W. S. Fegadolli, M. H. Lu, J. E. Oliveira, V. R. Almeida, Y. F. Chen, A. Scherer, *Nat. Mater.* **2013**, *12*, 108.

[9] Z. Lin, H. Ramezani, T. Eichelkraut, T. Kottos, H. Cao, D. N. Christodoulides, *Phys. Rev. Lett.* **2011**, *106*, 213901.

[10] Y. Xu, L. Li, H. Jeong, S. Kim, I. Kim, J. Rho, Y. Liu, *Sci. Adv.* **2023**, *9*, eadf3510.

[11] J. Doppler, A. A. Mailybaev, J. Böhm, U. Kuhl, A. Girschik, F. Libisch, T. J. Milburn, P. Rabl, N. Moiseyev, S. Rotter, *Nature* **2016**, *537*, 76.

[12] B. Peng, Ş. K. Özdemir, M. Liertzer, L. Yang, *Proc. Natl. Acad. Sci. U. S. A.* **2016**, *113*, 6845.

[13] J. Wiersig, *Phys. Rev. Lett.* **2014**, *112*, 203901.

[14] W. Chen, Ş. Kaya Özdemir, G. Zhao, J. Wiersig, L. Yang, *Nature* **2017**, *548*, 192.

[15] Q. Zhong, J. Ren, M. Khajavikhan, D. N. Christodoulides, Ş. K. Özdemir, R. El-Ganainy, *Phys. Rev. Lett.* **2019**, *122*, 153902.

[16] S. H. Park, S. G. Lee, S. Baek, T. Ha, S. Lee, B. Min, S. Zhang, M. Lawrence, T. T. Kim, *Nanophotonics* **2020**, *9*, 1031.

[17] S. Dong, G. Hu, Q. Wang, Y. Jia, Q. Zhang, G. Cao, J. Wang, S. Chen, D. Fan, W. Jiang, Y. Li, A. Alù, C. W. Qiu, *ACS Photonics* **2020**, *7*, 3321.

[18] S. Li, X. Zhang, Q. Xu, M. Liu, M. Kang, J. Han, W. Zhang, *Opt. Express* **2020**, *28*, 20083.

[19] Q. Song, M. Odeh, J. Zúñiga-Pérez, B. Kanté, P. Genevet, *Science* **2021**, *373*, 1133.

[20] J.-H. Park, A. Ndao, W. Cai, L. Hsu, A. Kodigala, T. Lepetit, Y. H. Lo, B. Kanté, *Nat. Phys.* **2020**, *16*, 462.

[21] F. Ma, Y. Li, B. Tang, C. Zhang, *Acc. Chem. Res.* **2016**, *49*, 1722.

[22] A. Gaiduk, P. V. Ruijgrok, M. Yorulmaz, M. Orrit, *Chem. Sci.* **2010**, *1*, 343.

[23] M. D. Baaske, M. R. Foreman, F. Vollmer, *Nat. Nanotechnol.* **2014**, *9*, 933.

[24] S. A. Maier, *Plasmonics: Fundamentals and Applications*, Springer, New York **2007**.

[25] A. B. Taylor, P. Zijlstra, *ACS Sens.* **2017**, *2*, 1103.

[26] K.-S. Lee, M. A. El-Sayed, *J. Phys. Chem. B* **2006**, *110*, 19220.

[27] K. M. Mayer, J. H. Hafner, *Chem. Rev.* **2011**, *111*, 3828.

[28] A. Pors, E. Moreno, L. Martin-Moreno, J. B. Pendry, F. J. Garcia-Vidal, *Phys. Rev. Lett.* **2012**, *108*, 223905.

[29] H. Su, X. Shen, G. Su, L. Li, J. Ding, F. Liu, P. Zhan, Y. Liu, Z. Wang, *Laser Photonics Rev.* **2018**, *12*, 1800010.

[30] J. Yang, X. Zheng, J. Wang, A. Zhang, T. J. Cui, G. A. E. Vandenbosch, *Laser Photonics Rev.* **2022**, *16*, 2100373,.

[31] G. Su, H. Su, L. Hu, Z. Qin, X. Shen, J. Ding, F. Liu, M. Lu, P. Zhan, Y. Liu, *Appl. Phys. Lett.* **2021**, *118*, 241106,.

[32] Z. Liao, J. N. Zhou, G. Q. Luo, M. Wang, S. Sun, T. Zhou, H. F. Ma, T. J. Cui, Y. Liu, *Phys. Rev. Appl.* **2020**, *13*, 054013.

[33] Z. Liao, Y. Che, L. Liu, B. C. Pan, B. G. Cai, J. N. Zhou, G. Q. Luo, Y. Liu, *IEEE Trans. Antennas Propag.* **2022**, *70*, 6795.

[34] J. Yang, X. Zheng, J. Wang, Y. Pan, A. Zhang, T. Cui, G. A. E. Vandenbosch, *Laser Photonics Rev.* **2022**, *16*, 2200007,.

[35] Z.-L. Deng, T. Shi, A. Krasnok, X. Li, A. Alù, *Nat. Commun.* **2022**, *13*, 8.

[36] X. Li, L. Liu, Z. Zhou, J. Shen, Y. Zhang, G. Han, Z. Li, *Adv. Opt. Mater.* **2022**, *10*, 2200331,.

[37] T. H. Arikawa, S. Morimoto, F. Blanchard, S. Tani, T. Tanaka, K. Sakai, K. Sasaki, K. Tanaka, *Sci. Adv.* **2020**, *6*, 1977.

[38] L. Chen, N. Xu, L. Singh, T. Cui, R. Singh, Y. Zhu, W. Zhang, *Adv. Opt. Mater.* **2017**, *5*, 1600960.

[39] H. Jiang, W. Zhang, G. Lu, L. Ye, H. Lin, J. Tang, Z. Xue, Z. Li, H. Xu, 0 Gong, *Photonics Res.* **2022**, *10*, 557.